JOURNAL OF MATERIALS SCIENCE 32 (1997) 3143–3156

Effect of initial microstructure on high velocity and hypervelocity impact cratering and crater-related microstructures in thick copper targets

Part II *Stainless steel projectiles*

L. E. MURR, C-S. NIOU, E. FERREYRA T., E. P. GARCIA, G. LIU
Department of Metallurgical and Materials Engineering, The University of Texas at El Paso, El Paso, Texas 79968, USA

F. HÖRZ
Solar System Exploration Division, NASA-Johnson Space Center, Houston, Texas, 77058, USA

R. P. BERNHARD
Lockheed-Martin Engineering Sciences, C23, Houston, Texas 77058, USA

Three different, thick copper targets (an as-received, 98 μm grain size containing $\sim 10^{10}$ dislocations/cm^2 (Vickers hardness of 0.89 GPa); an annealed, 124 μm grain size containing 10^9 dislocations/cm^2 (Vicker's hardness of 0.69 GPa); and a 763 μm grain size containing 10^9 dislocations/cm^2 (Vickers hardness of 0.67 GPa) were impacted with 3.18 mm diameter ferritic stainless steel projectiles at nominal velocities of 0.7, 2 and 5 km s^{-1}. Like companion experiments utilizing soda-lime glass projectiles (Part I), absolute grain size of the target was observed to be less important than the dislocation density in the cratering process. At low impact velocity, depth/diameter ratios were observed to increase dramatically in contrast to less dense soda-lime glass impactors, and the impactor behaviours were also very different. The ferritic stainless steel impactors spalled into small fragments at or above 2 km s^{-1} impact velocity and a significant fraction of these fragments remained in the craters. No significant melt phenomena were observed either in connection with projectile fragmentation or in the crater-related, residual microstructures. Dynamic recrystallization, dislocation cell structures and microbands were significant microstructural features in the targets. They extended from the crater walls and contributed to hardness profiles within the cratered targets. These hardness profiles and actual hardness zones generally increased in extent from the crater wall with both impact velocity and projectile density.

1. Introduction

In Part I [1] of this two-part study, we demonstrated for the first time that the initial target microstructure, especially the density of dislocation structures, has a measurable influence on hypervelocity impact cratering. We employed copper targets having an initial grain size varying from about 98 to 124 μm, but with a dislocation density variation by an order of magnitude (from 10^{10} to 10^9 cm^{-2}) and an average Vickers microhardness for the target ($H_{t(o)}$) which varied from 89 to 69 VHN, respectively. This corresponded to actual ratios of crater diameter to projectile diameter, $(D_c/d_p)/(D_c/d_p)$, for the hardest/softest targets, respectively, of 0.97, over a range of impact velocities from 2 to 6 km s^{-1} for soda-lime glass spheres of $d_p = 3.2$ mm. The theoretical ratio of $[H_{t(o)}(\text{softest})/H_{t(o)}(\text{hardest})]^{1/3} \cong (69/89)^{1/3} \cong 0.92$ (from Equation 4 in Part I [1]) or a difference of 5% based on the experimental data (= 0.97) since $D_c/d_p \propto 1/H_t^{1/3}$ [1].

In Part I, craters formed at impact velocities of roughly 2, 4 and 6 km s^{-1} for 3.2 mm diameter soda-lime glass spheres ($\rho_p = 2.2$ g cm^{-3}) into each of three microstructurally distinct copper targets ($\rho_t = 8.9$ g cm^{-3}) exhibited unique microstructures, corresponding to specific VHN, extending outward from the crater walls. The extent and density of specific target microstructures included a zone of dynamically recrystallized grains at the crater bottom and walls and a more extensive zone of microbands, generally increasing with increasing impact velocity for all

0022–2461

initial target conditions. There was only meager evidence for impacting projectile (soda-lime glass) residues within any craters formed over this velocity range, and there was no significant evidence for melt phenomena either adjacent to the crater wall or within the jetting regime forming the associated crater rims. We refer to jetting as the differential flow or displacement (in the solid-state) of material at the crater surface into the rim. Some of this material can become detached and ejected. While microstructures, especially the occurrence of microbands in regions beyond the crater wall, were clearly altered (increased) with increasing impact velocity and grain size, it was unclear whether this was impact pressure dependent, even though the pressures (both the plane-wave shock or Hugoniot pressure (P_S) and the so-called steady-state Bernoulli pressure (P_B)) increased with increasing impact velocity, u_o, from 24 to 108 GPa (P_S) and from 2 to 18 GPa (P_B), respectively, at 2 and 6 km s^{-1}.

In this (Part II) study, we extend the observations of target and crater-related microstructural issues described in Part I [1] into higher pressure regimes, albeit at relatively low velocities, by utilizing 3.2 mm nominal diameter ferritic stainless steel projectiles ($\rho_p = 7.86$ g cm^{-3}). Steady-state (Bernoulli) pressures ranged from 0.5 to 30 GPa.

While these extended experiments do not address the specific concept of supralinearity through variations of the impacting projectile diameter, d_p, or corresponding crater diameters, D_c, in relation to the target grain sizes, the significantly greater projectile density and associated impact pressures were assumed to produce even more exaggerated differences in cratering. This would support or augment the previous observations and conclusions about target microstructures affecting both the cratering process and the associated, residual, crater-related microstructures created in specific, experimental targets. Furthermore, the high strength and high melting temperature associated with stainless steel projectiles were considered to have the potential to provide a different view of projectile behaviour during the cratering process in contrast to the soda-lime glass projectiles utilized in the previous (Part I) study [1].

2. Experimental details

The experimental details and procedures have generally been described in Part I [1]. Table I and Fig. 1 of Part I [1] provide the details for the target plate variations examined with respect to soda-lime glass spheres impacting at nominal velocities of 2, 4 and 6 km s^{-1}. In this extension (Part II) of these earlier investigations carefully selected (3.18 mm diameter) ferritic stainless steel spheres (nominally 29 wt% Cr, balance Fe; $\rho_p = 7.86$ g cm^{-3}) were impacted as noted previously [1] into each of the three experimental copper target plates: A, as-received, 0.89 GPa hardness, grain size of 98 μm; B, annealed, 0.69 GPa hardness, grain size of 124 μm; C, annealed, 0.67 GPa hardness, grain size of 763 μm. Nominal impact velocities ranged from roughly 0.7 to 5 km s^{-1} utilizing laboratory gun facilities described previously [1]. The impact craters were carefully photographed and also examined in detail in the scanning electron microscope (SEM) (an ISI DS-130 SEM). There were no observations of near-surface target spallation even at the highest impact velocity. The fully documented craters were then carefully cut with a high-speed diamond saw to expose exact half sections in order to make accurate measurements of the crater geometry, and to allow for more detailed examination of the crater half-sections in the SEM. Crater half-sections were polished for light microscopy examination and the recording of Vickers microhardness profiles extending from the crater bottom along the impact axis as in Part I [1]. Transmission electron microscopy (TEM) imaging of strategically extracted and electropolished disc sections from specific locations beyond the crater wall, and within the target, was also performed utilizing a Hitachi H-8000 analytical transmission electron microscope, operated at 200 kV.

3. Results

Figs 1 and 2 show for comparison the complete series of impacts in targets A to C (the mill-processed (A) and mill-processed and annealed targets (B and C)), respectively, which correspond to grain sizes of 98 to 763 μm, respectively, and average microhardnesses of 0.89 (A) and 0.67 (C) GPa, respectively. Geometries for these experimental craters (Figs 1 and 2), measured as described in Fig. 2c of Part I [1], are listed in Table I (crater diameter, D_c, depth of penetration, p, and associated ratios) which also includes the associated impact velocities and calculated pressures from Equations 1 and 2 of Part I [1, 2]. In contrast to the soda-lime glass induced craters in Part I [1], Figs 1 and 2 illustrate considerably different cratering phenomena, especially in the context of the projectile behaviour and projectile residue within the craters. In both Fig. 1 and Fig. 2a and d corresponding to the lowest impact velocities, respectively, the stainless steel projectile remained essentially intact except for two-fold symmetric, intersecting horizontal and vertical spall cracks.

This projectile spall symmetry attests to the shock geometry and symmetric shock wave reflection from the base of the projectile at the instant of impact. The steady-state (Bernoulli) pressure was only 0.5 to 0.6 GPa for these craters. There is a particularly notable penetration into the B target at 0.78 km s^{-1} impact velocity (higher than the A and C targets), and a correspondingly higher p/D_c ratio (Table I). However, both the softer B and C targets exhibited a higher penetration and p/D_c ratio than the A target, consistent with the observations for the lowest impact velocities in Part I [1] for soda-lime glass induced craters.

In contrast to the intact projectiles shown in Figs 1 and 2a and d, the higher velocity craters in Figs 1 and 2b to d exhibited somewhat differing degrees of projectile spall fragmentation (due in part to the brittle nature of this ferritic stainless steel, which also contained a few per cent aluminium for at least one projectile). There appeared to be more fragments and

somewhat larger fragments within the crater at the medium velocity ($\sim 2\,km\,s^{-1}$) in contrast to the highest velocity ($\sim 5\,km\,s^{-1}$) (compare Fig. 1). In addition, the projectile fragments appeared to be embedded within the crater walls and jetted out onto the rim surface regions (Fig. 2e). These features are illustrated more clearly in the views shown in Fig. 3. Fig. 3 also shows the large projectile spall cone at the base of the craters in section view, and in contrast to the normal view shown in Fig. 2c and f. Many projectile spall fragments have a conical fracture surface as a consequence of the spherical shock geometry in the spherical projectile, and these spall fragments have been thrown against the forming crater wall. Projectile spall fragments have even been carried out onto the crater rim as shown in Figs 2e, 3b and d. Fig. 3d illustrates

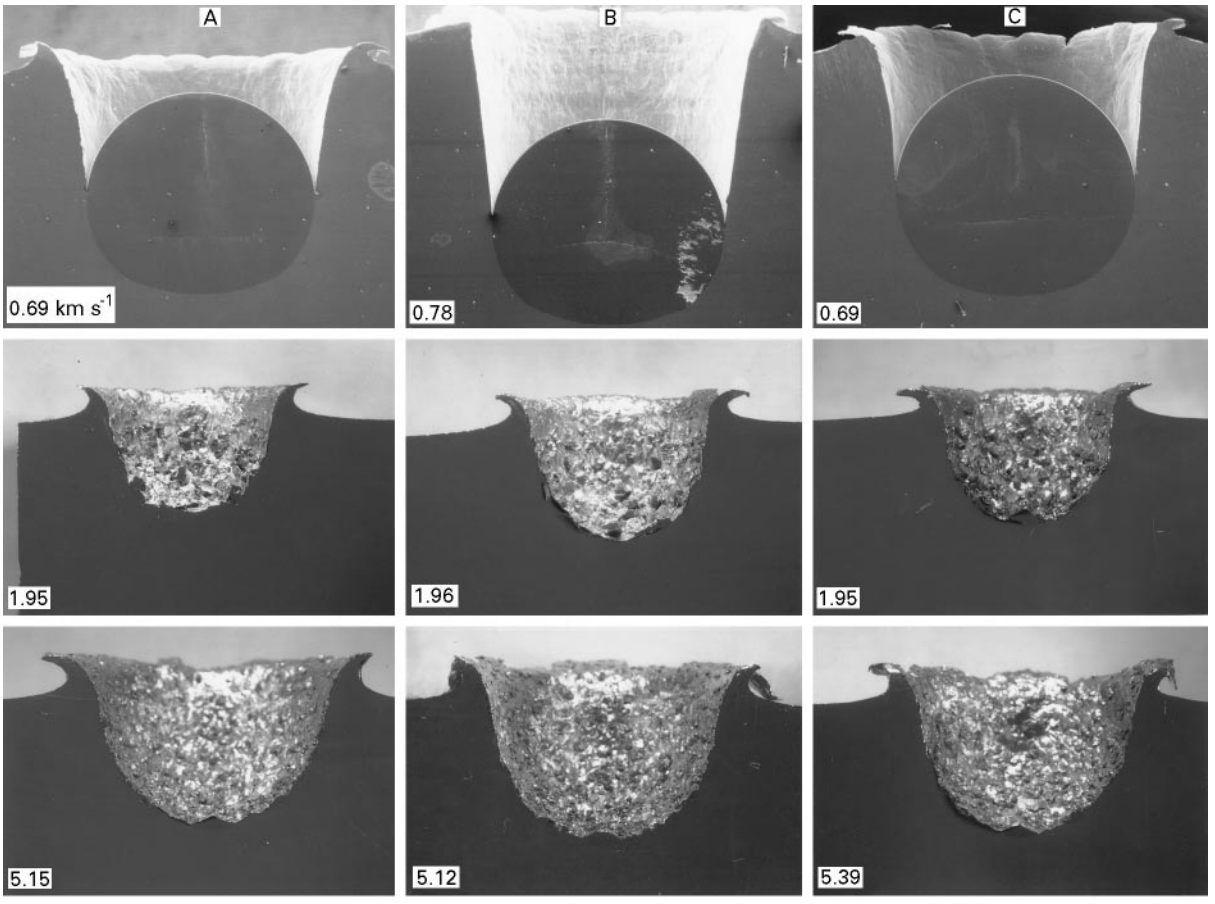

Figure 1 Cross-section (optical) views of craters produced by 3.18 mm diameter ferritic stainless steel projectiles impacting different copper targets (A, B and C) at velocities noted in each view (lower left in $km\,s^{-1}$). See Table I for target specifications and crater dimensions.

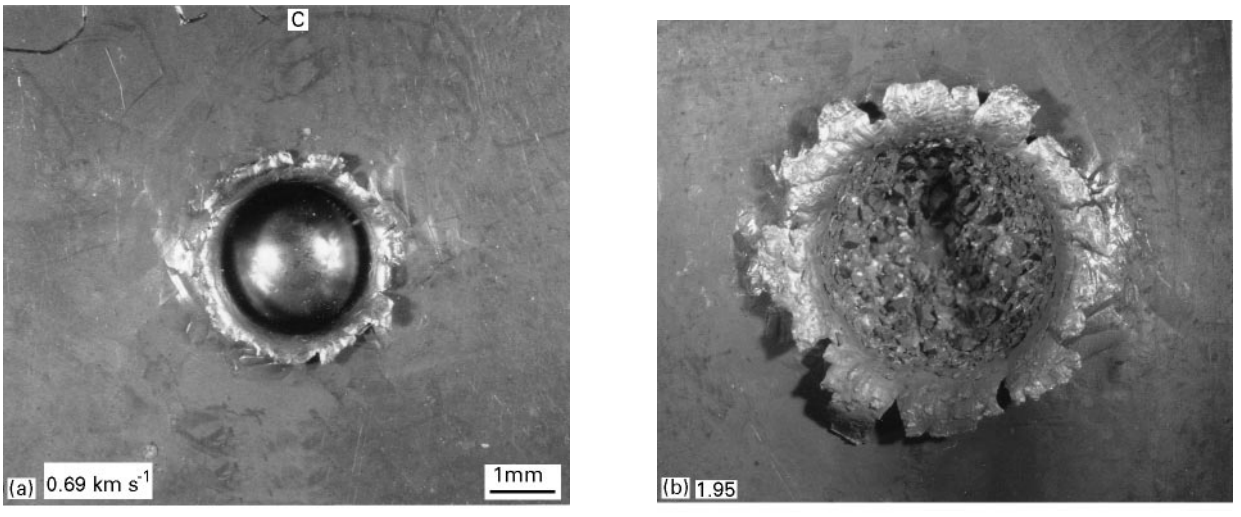

Figure 2 Normal (plan) views of craters in annealed (C) ((a) to (c)) and (B) (d) copper targets, at impact velocities shown for 3.18 mm diameter ferritic stainless steel projectiles. (e) Shows an enlarged SEM view of projectile fragments on rim surface shown near arrow in (c). (f) Shows an SEM enlargement of conical projectile fragment in centre of crater base in (c). Magnifications (a) to (c) are shown in (a).

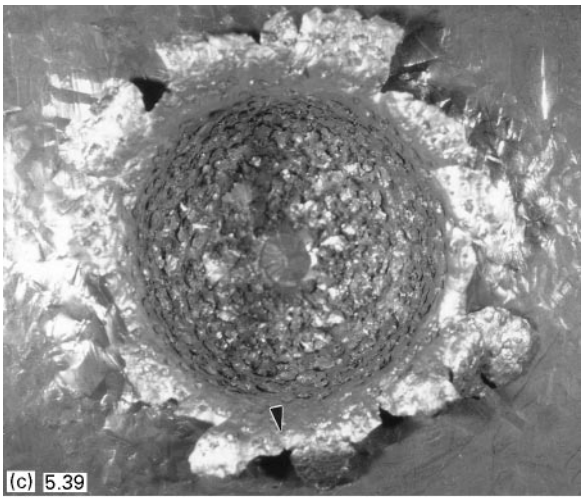

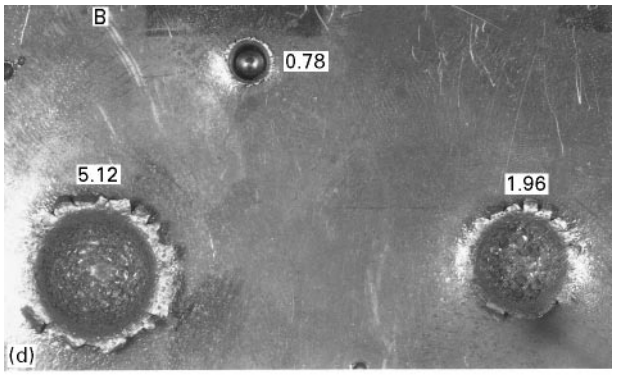

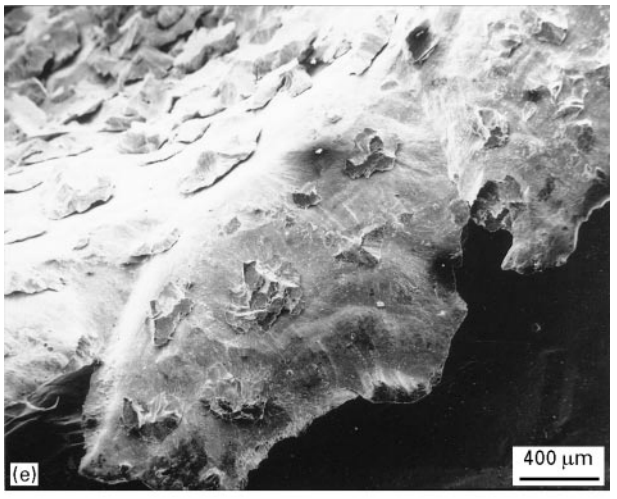

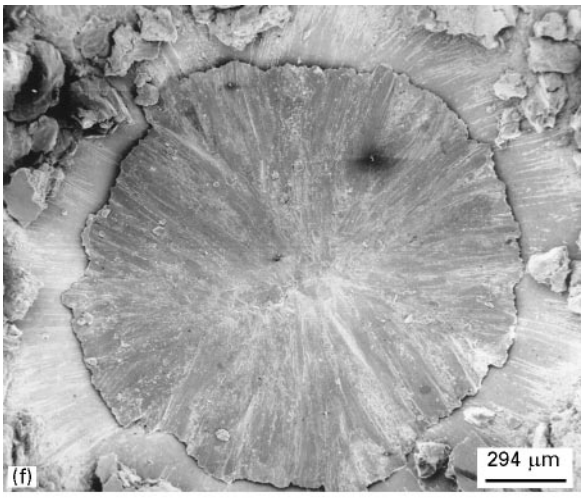

Figure 2 (Continued).

TABLE I Experimental impact crater parameters and geometries (3.18 mm nominal diameter (d_p) ferritic stainless steel spheres impacting OFHC copper targets)

Target[a]	u_o (km s^{-1})	p (mm)	D_c (mm)	p/D_c	D_c/d_p	P_s^b (GPa)	P_B^a (GPa)
Low-velocity impact craters							
A	0.69	3.05	3.7	0.82	1.16	14	0.5
B	0.78	3.92	3.89	1.0	1.22	16	0.6
C	0.69	3.32	3.56	0.93	1.12	14	0.5
Medium-velocity impact craters							
A	1.95	4.55	8.0	0.57	2.52	47	4
B	1.96	5.45	8.5	0.64	2.67	47	4
C	1.95	5.06	8.1	0.62	2.55	47	4
High-velocity impact craters							
A	5.15	6.24	10.7	0.59	3.36	175	28
B	5.12	6.76	11.1	0.61	3.49	173	27
C	5.39	6.37	10.6	0.60	3.33	187	30

[a] A: mill-processed, 2.5 cm thick plate, 98 μm grain size, 0.89 GPa Vickers hardness.
B: mill-processed, annealed (500 °C, 2 h), 2.5 cm thick plate, 124 μm grain size, 0.69 GPa Vickers hardness.
C: mill-processed, annealed (1000 °C, 10 h), 2.5 cm thick plate, 763 μm grain size, 0.67 GPa Vickers hardness.
The copper target density was 8.9 g cm^{-3}. The ferritic stainless steel impacting spheres had a density of 7.86 g cm^{-3}.
[b] P_s is the instantaneous, peak shock pressure calculated using the plane-wave shock Hugoniot approximation (see Equation 1, Part I [1]) [2].
[c] P_B is the steady-state, Bernoulli pressure, often considered to be the shock pressure at the crater base when it is fully formed (see Equation 2, Part I [1]).

features of mechanical alloying or bonding with the crater rim region to affect a metallurgical bond. Energy-dispersive X-ray spectrometry at the base region of the particle in Fig. 3d has supported these conclusions.

Fig. 4 shows the comparative, residual microhardness profiles extending along the impact axes from the crater wall bottoms for each specific impact velocity in the corresponding copper targets (A, B and C, respectively). It can be observed in Fig. 4 that the extent of residual hardening outward from the crater wall is generally more extensive for the softer targets (B and C). In fact, the hardness for the C target at 2 and 5.4 km s^{-1} impact velocities remains above the base target hardness throughout the entire target thickness. The extent of softening at or near the crater wall is greater in the A target but the degree of softening is greatest in the C target at the highest velocity (5.39 km s^{-1}). There is a rather notable difference between the hardness profiles for the stainless steel projectiles in Fig. 4 in contrast to the soda-lime glass projectiles in Fig. 4 of Part I [1]. There is generally less softening for stainless steel in contrast to soda-lime glass projectiles and the highest velocity impacts do not exhibit the maximum softening even though the dynamic recrystallization zone is more extensive. This is particularly notable for the large-grain, annealed target (C) where the recrystallized zone width for the highest velocity soda-lime projectile crater was around 0.2 to 0.3 mm while the recrystallized zone width for the highest velocity stainless steel projectile

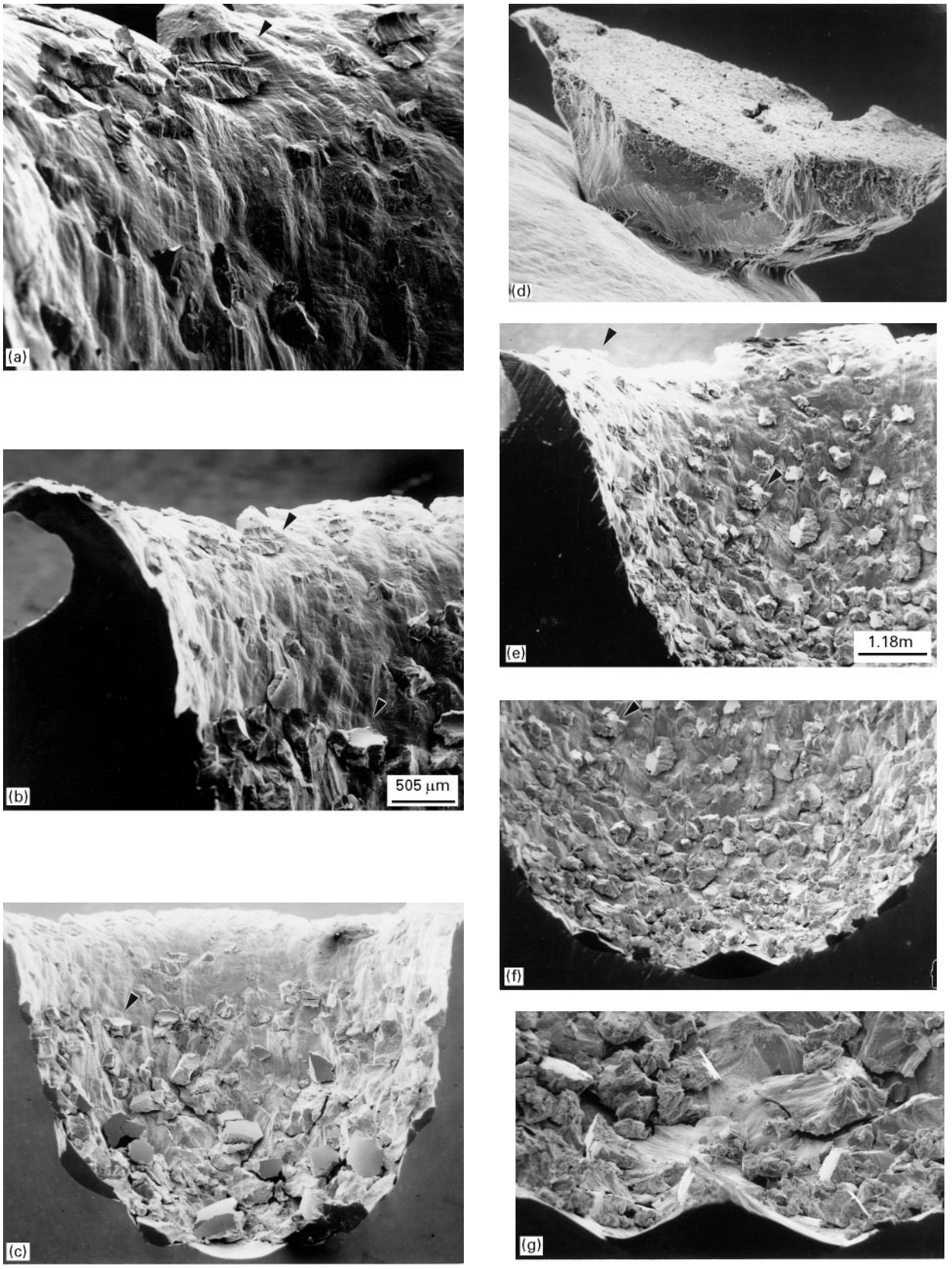

Figure 3 SEM views of crater cross-sections showing residual, deposited ferritic stainless steel projectile fragments. (a) and (b) show upper portion, including the rim, for the 1.96 km s^{-1} impact crater in the B target (c). The arrows in each figure (a) to (c) provide continuity references. (d) through (g) show a similar cross-section sequence for the 5.12 km s^{-1} impact crater in the B target. Note conical projectile fragment at the crater base in (g). The rim fragment in (d) is shown at the arrow in (e).

crater was around 0.3 to 0.6 mm. The highest velocity impact craters (> 5 km s^{-1}) also exhibit extensive hardening associated with each target (A to C) in Fig. 4. Unlike the hardness curves of Fig. 4 of Part I [1] for the highest velocity of impact (~ 6 km s^{-1}) where the hardness is equal to the base target hardness between about 9 and 11 mm from the crater base, the hardness equals the base hardness between about 12 and 17 mm for the (~ 5 km s^{-1}) ferritic stainless steel projectile craters in Fig. 4. Consequently, the target

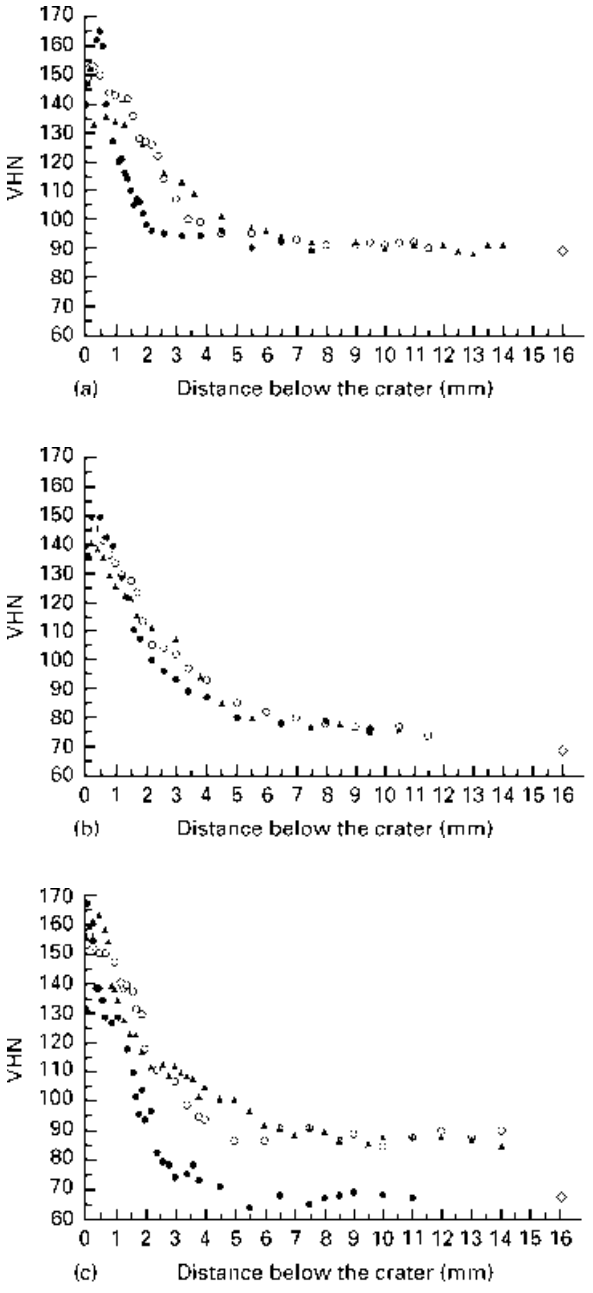

Figure 4 Residual hardness profiles for each experimental crater produced by ferritic stainless steel projectiles impacting copper targets noted, extending from the crater floor (at zero) along the impact axis. The hardness profiles are grouped according to impact velocity for each of the three experimental targets denoted A, B and C corresponding to designations in Table I. Hardness is in Vickers Hardness Number (VHN) which is equivalent to 10^{-2} GPa. (a) target A, (b) target B and (c) target C. Key: (a) ▲ 5.15 km s^{-1}, ○ 1.95 km s^{-1}, ● 0.69 km s^{-1}, ◇ base hardness; (b) ▲ 5.12 km s^{-1}, ○ 1.96 km s^{-1}, ● 0.78 km s^{-1}; ◇ base hardness; (c) ▲ 5.39 km s^{-1}, ○ 1.95 km s^{-1}, ● 0.69 km s^{-1}, ◇ base hardness.

hardening due to cratering generally increases both with velocity of impact as well as projectile density. The softest and largest grain size targets also promote more extensive residual hardening.

The narrower zone of softening near the crater wall generally observed in Fig. 4, as well as the overall, residual hardening trends reflected in Fig. 4, are noticeably different from those observed for soda-lime glass projectile impact craters (Fig. 4 of Part I [1]). These differences are illustrated in the comparative views of the crater-related microstructures shown in Fig. 5 for the hardest (A) and softest target (C); and the corresponding lowest (~ 0.7 km s^{-1}) and highest (~ 5.2 km s^{-1}) nominal impact velocity craters. While there is a recognizable zone of dynamic recrystallization next to the crater walls in Fig. 5, the zone is less extensive for the lowest velocity craters, and more extensive for the highest velocities than for soda-lime glass impact craters formed at even higher velocities (in Part I [1]). There was evidence for more extensive grain growth associated with the dynamic recrystallization and there were observations of thin twins within the recrystallized and grain growth regions near the crater walls. Furthermore, while there is extensive microbanding and a zone of microbands beyond the dynamic recrystallized zone, there are also microbands at the crater wall for the lowest velocity crater in the softest target (C). The extent of microbands associated with the hypervelocity impact crater on the softest target (C) was observed to be about 20% greater than the corresponding soda-lime glass hypervelocity impact crater in Part I [1]. There also seemed to be more microbands and more dense bands in Fig. 5. Some of these features are illustrated in Fig. 6 for microbands located about 0.3 mm from the 5.39 km s^{-1} crater side walls in the softest target (C). Fig. 6 also illustrates the heterogeneous serrations created on low-energy annealing twin boundaries through the extreme and localized shear stresses which create the microbands in $\{1\,1\,1\}$ trace directions. These are common observations and have also been shown in Fig. 7 of Part I [1]. These features, along with related, dislocation cell structures which extend into the targets in Fig. 5, are illustrated in the representative TEM images in Fig. 7. The microstructures shown in Fig. 7 are typical of those observed in Part I [1] and previous cratering studies in copper targets [3–6]. They include recrystallized grains or dynamic recrystallization microstructures (DRX), at the crater wall which intermix with dislocation cells (DC) and microbands (MB). Beyond the microbands, or at distances beyond which microbands are no longer observed in the target, dislocation cells are observed to increase in size, and the dislocation density generally decreases until the base target microstructure occurs. However, in the C target at 5.39 km s^{-1} impact velocity, dislocation cells persist up to the target rear surface, consistent with the hardness data shown in Fig. 4.

4. Discussion

It can be observed from Table I that cratering of ferritic stainless steel projectiles follows the same trends established for soda-lime glass projectiles into copper targets with varying microstructures and corresponding hardnesses: penetration depth, p, and p/D_c ratios are less for the mill-annealed, hardest target than for the softer, annealed targets in spite of some obvious irregularities in the penetration behaviour between the softest targets (B and C). It is not known, for example, why the penetration is so noticeably different for the B target in comparison to the C target

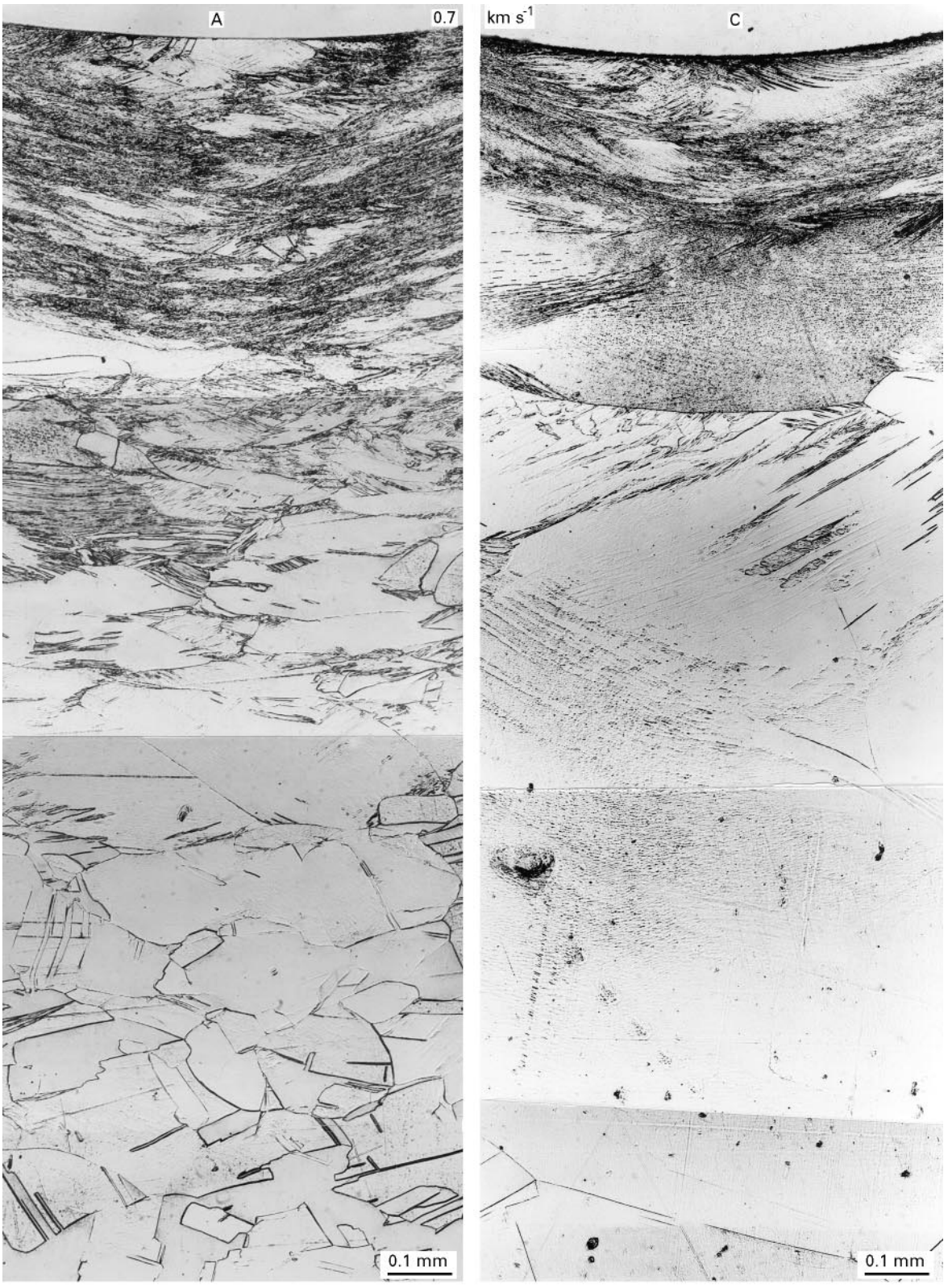

Figure 5 Light microscope sequences corresponding to narrow strips along the impact axes and below specific crater bottoms for ferritic stainless steel (3.18 mm diameter) spheres impacting at the lowest and highest velocities into targets noted (A and C).

at the lowest velocity (Fig. 1). However, the ratio p/D_c is progressive at 2 and 5 km s^{-1} nominal velocities.

It is observed in Table I that the general trends in cratering observed in Part I [1] for soda-lime glass projectile impacts are also observed for the ferritic stainless steel projectile impacts: the crater depth, p, increases in the softer targets (B and C or between A and B in particular) and the ratios of (D_c/d_p)/(D_c/d_p) for the hardest/softest (A/C) targets were observed to be approximately unity (1.0) for all impact velocities. This is in contrast to a theoretical (ideal) ratio of 0.92 [1]. Like the soda-lime glass impact craters, the ferritic stainless steel impact craters show a greater difference in crater depth between the different target hardnesses (A to B) at the lower velocities than the highest velocity (29% and 20% for

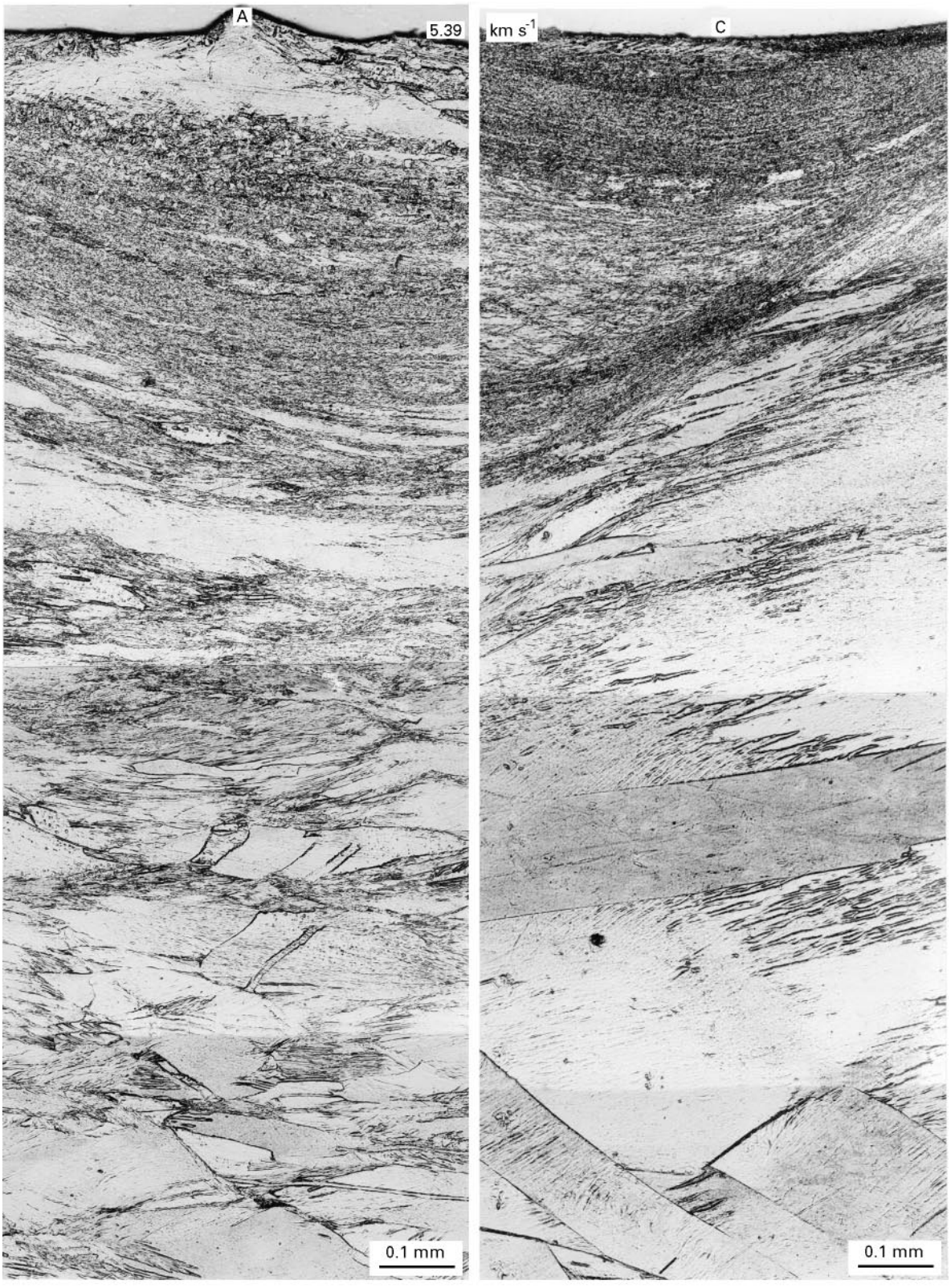

Figure 5 (Continued).

0.7 km s^{-1} and 2 km s^{-1} in contrast to ~8% for 5 km s^{-1} in Table I).

Fig. 8 shows comparison plots of p/D_c versus impact velocity for the 3.18 mm diameter soda-lime glass projectiles (from Table II of Part I [1]) and the 3.18 mm diameter ferritic stainless steel projectiles from Table I, for each different target: A, B and C. The variations in p/D_c for the hardest (A) targets in contrast to the softer (B and C) targets are shown shaded. It can be noted that while the variations are similar (that is the trends are similar), there are marked differences for the more dense, ferritic stainless steel projectiles not only in terms of target cratering geometry variations, but also in the upward shift of p/D_c values, and the extreme divergence of p/D_c values for the two different densities of projectiles at low impact

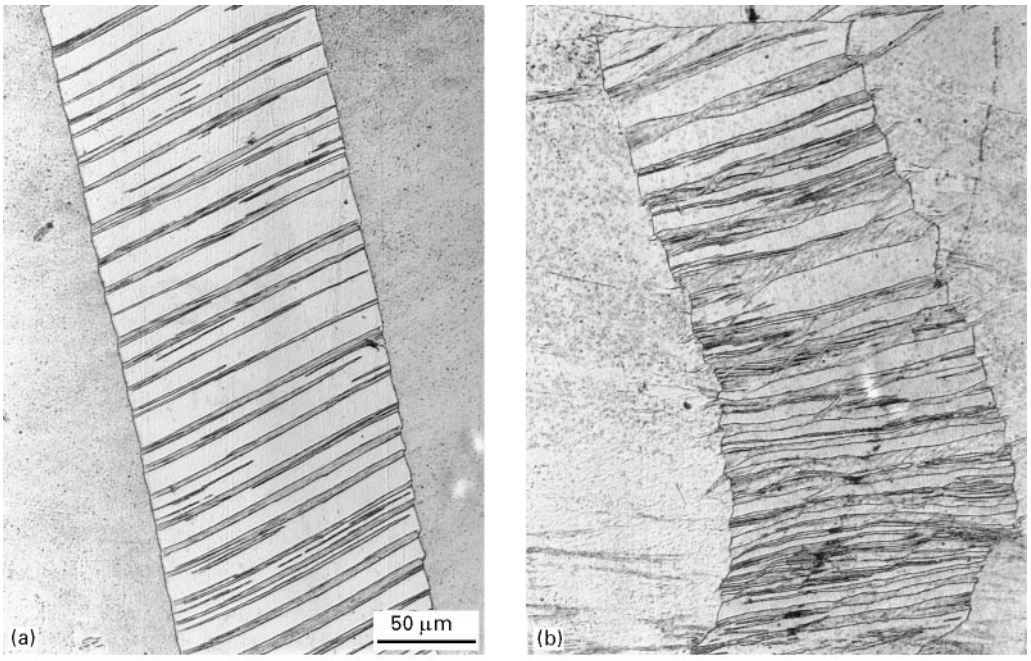

Figure 6 Dense microbands creating severe serrations along coherent annealing twin boundaries which they intersect (a). In (b), there is a corresponding deformation of the serrated annealing twin. Both (a) and (b) correspond to regions near the crater wall in the 5.39 $km\,s^{-1}$ impact crater in the annealed (C) copper target.

velocities ($< 2\,km\,s^{-1}$). The validity of this divergence is strengthened by the inclusion of recent data of Quinones *et al.* [4] for 1100 aluminium projectiles (of the same diameter: 3.18 mm) impacting small grain (38 μm) copper targets with an average hardness of 0.82 GPa. The low-velocity regime peak of p/D_c noted in Fig. 8 for the more dense stainless steel projectiles is similar to the response of 1100 aluminium targets to soda-lime glass projectile impacts of the same size (3.18 mm) as those observed in Fig. 8, recently illustrated by Bernhard and Hörz [7]. A similar upward trend and narrow peak of values of p/D_c versus u_o was also noted for steel projectiles into 1100 aluminium targets by Baker [8], where p/D_c values exceeded 1.1 in contrast to about 0.8 for soda-lime glass projectiles into 1100 aluminium [7].

This low velocity impact behaviour, and in particular the differences noted in Fig. 8, would appear to be related to the density ratio, ρ_p/ρ_t, or some critical density ratio above which the low-velocity cratering behaviour differentiates itself significantly from hypervelocity behaviour. It can be noted that the low-density projectile impact data in Fig. 8 converges toward a p/D_c ratio between about 0.35 and 0.45 which is less than a hemispherical crater, while the high-density projectile impact data converges toward a p/D_c ratio between roughly 0.55 and 0.65, or slightly greater than a hemispherical crater where $p/D_c = 0.5$. The reason for the change in cratering behaviour illustrated in Fig. 8 is not really understood, and suggests the need for more extensive cratering studies of various targets over a range of projectile densities or ρ_p/ρ_t values. In more descriptive, empirical terms, the soda-lime glass and aluminium impactors are more deformed at $\sim 1\,km\,s^{-1}$ whereas the stainless steel impactors are not. This may be the real difference between "physical properties" and hydrodynamic behaviour of either impactor or target, or both. Fundamental differences in the actual plastic flow and target material displacement during cratering at 0.7 $km\,s^{-1}$ versus 5.4 $km\,s^{-1}$ suggested in Fig. 8 for the stainless steel projectile data is, to some extent, reflected in the comparative views of the crater-related microstructures shown in Fig. 5. Particularly notable for the low-velocity microstructures is the narrow zone of dynamic recrystallization and the occurrence of microbands very near, or extending from, the crater wall into the target. There is a general absence of shock-induced microstructures and only a narrow zone involving plastic deformation in contrast to a more extended region of deformation microstructures, including microbands and dislocation cells, in the higher velocity impacts. It is interesting to note that in earlier studies of particle erosion of copper surfaces, where impacting particles had velocities around 0.06 $km\,s^{-1}$ or less, the underlying microstructures in the targets illustrated a very narrow zone of dynamic recrystallization (~ 2 μm) and dislocation cell structures which increased in size like those observed for cratering, although the zone thickness was considerably smaller [9–11]. Deformation twins have also been observed in these studies [11], but no microbands.

The differences apparent in Fig. 8 for specific target microstructures and corresponding hardnesses, are also apparent in the comparative data illustrated in Fig. 9 from the hardness curves for the stainless steel projectiles (Fig. 4) and the soda-lime glass projectiles in Fig. 4 of Part I [1]. Fig. 9 shows the distance, Δ, from the crater wall for each corresponding impact velocity and target, where the hardness becomes equal (approximately) to the base target hardness. Only the hardest (A) and softest (C) target data is included in Fig. 9 and only the lowest ($2\,km\,s^{-1}$) and highest

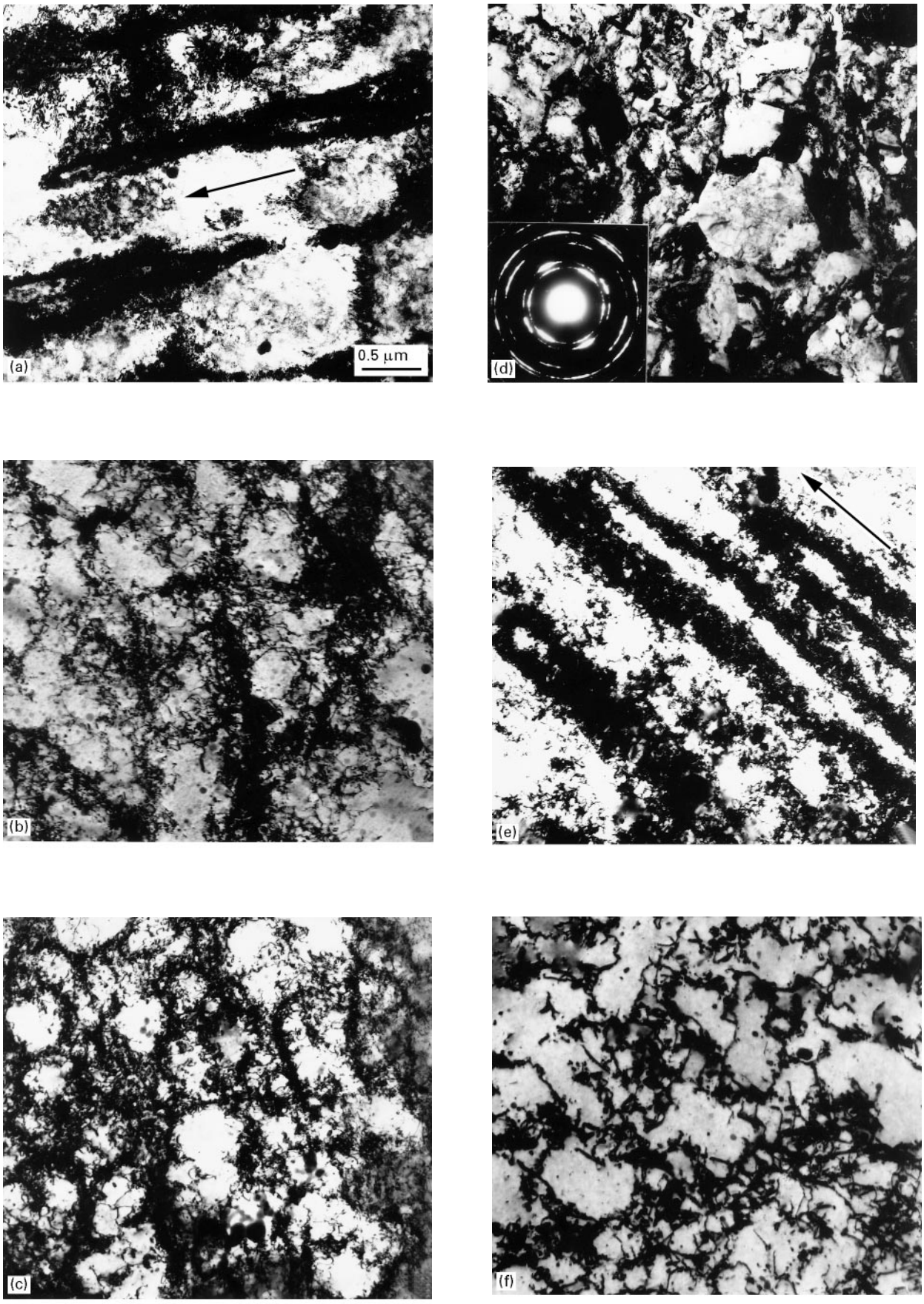

Figure 7 TEM image examples of prominent microstructural features associated with the 0.7 km s^{-1} ferritic stainless steel projectile impact (left) and the 5.4 km s^{-1} ferritic stainless steel projectile impact (right), into the annealed C copper target. (a) Dense microbands located roughly 0.1 mm from the crater wall. (b) Dense dislocation cells at a distance of 2 mm from the crater wall. (c) Dislocation cells at a distance of 3 mm from the crater wall. (d) Dynamic recrystallization DRX observed at about 0.1 mm from the crater wall. SAD pattern insert shows reflection rings characteristic of small, random grain structure. (e) Dense microbands located approximately 3 mm from the crater wall. (f) Dense dislocation cell structures at a distance of roughly 7 mm from the crater wall. In (a) and (e) the microband coincidence with the trace of $\{1\,1\,1\}$ is indicated by the arrow.

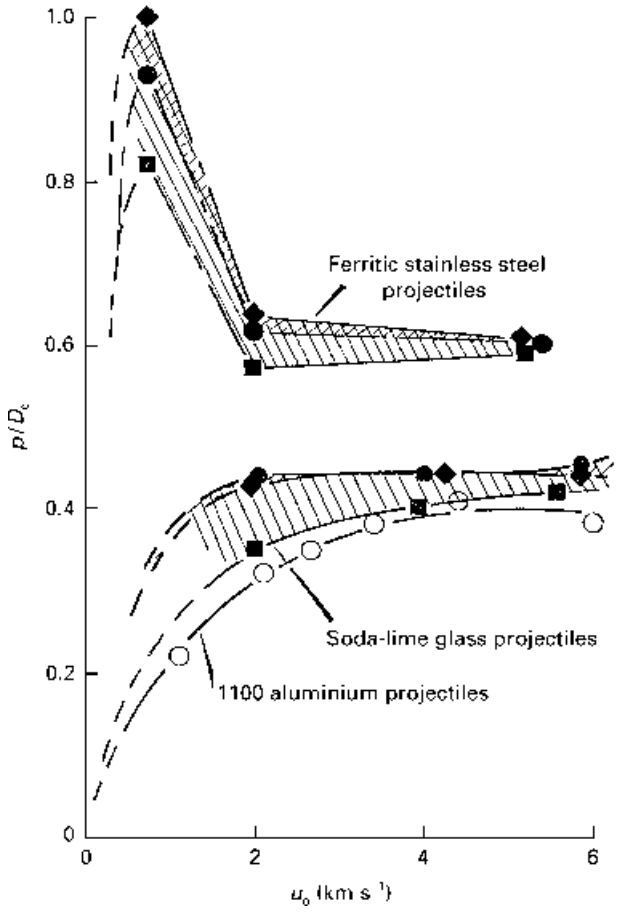

Figure 8 Comparison of the experimental crater depth/diameter (p/D_c) ratios versus projectile impact velocity (u_o) for same size (3.18 mm diameter) ferritic stainless steel projectiles, soda-lime glass projectiles and 1100 aluminium projectiles (from Quinones *et al.* [4]) for various copper targets: A, B and C. The 1100 aluminium projectile data corresponds to a 38 μm grain size copper target with a hardness of 0.82 GPa (Vickers). The shading accentuates the differences between specific target types. Key: ■ A (0.89 GPa); ◆ B (0.69 GPa); ● C (0.67 GPa).

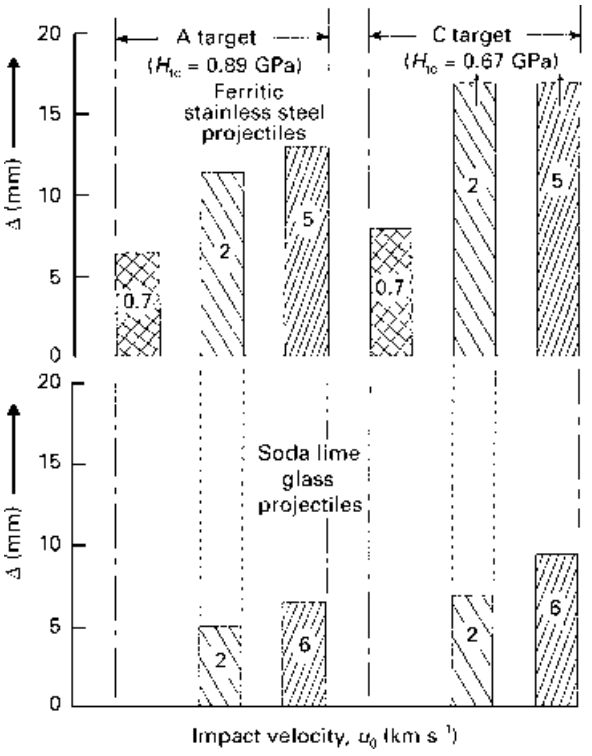

Figure 9 Bar graph comparisons of the maximum extent of residual hardening (△) along the impact axis for ferritic stainless steel projectile impacts and soda-lime glass projectile impacts into A and C copper targets at nominal velocities noted within each bar (in km s^{-1}). △ in mm is defined as the distance from the crater wall where $H_t = H_{t(o)}$ (the base target hardness value) (from data in Fig. 4 and Fig. 4 of Part I [1]). Only the 2 km s^{-1} impact velocity is common to both projectile series (dotted connection).

(6 km s^{-1}) velocity data are shown for the soda-lime glass projectile impact craters. All of the velocities for stainless steel projectile impacts are shown in Fig. 9. There is a marked difference between the two categories of targets as well as the velocities for each projectile, and between the projectile regimes, consistent with the implications of Fig. 8. In addition, the extent of residual target hardening increases rather dramatically with impacting projectile density. The implications in Fig. 9 are that for dense projectile hypervelocity impacts even in dense targets such as copper, there can be considerable effects on the target microstructure (and hardness) in a zone far removed from the crater itself. Furthermore, the trends and approximate target zone boundary extent or dimensions (Δ) established in Fig. 9 could begin to provide some verification and adjustments to hydrocode models [12], which could be effectively used to predict target behaviour over a range of impact conditions in the hypervelocity regime more characteristic of space environments, especially low-Earth orbit ($u_o \geqslant 8$ km s^{-1}).

In addition to simple zone dimensions or microhardness demarcations with the target, it may be possible to include the target microstructure or corresponding hardnesses in model calculations as suggested in the comparative data of Fig. 9. These features, when combined with residual target microstructural observations, might be illustrated phenomenologically as shown in the schematics of Fig. 10 which serve to summarize the implications of results represented generally in Fig. 8, and the microstructural details presented in this paper and in Part I [1].

Finally, we should comment on the stainless steel projectile (impactor) behaviour, especially in the context of other, recent projectile or projectile (impactor) residue phenomena [7]. It is observed in Figs 1 to 3 that a considerable fraction of the projectile remains in the craters. Of course at the lowest velocity (0.7 to 0.8 km s^{-1}), the entire projectile remains in the craters. Only systematic vertical and horizontal spall cracks through the projectiles are observed. However at 2 and 5 km s^{-1} nominal velocities, the projectiles are completely and systematically spall fractured into similar-sized fragments, many possessing conical segments extending from the original, polished and curved projectile surface. These fragments appear to have been "welded" to the crater wall in some cases and jetted out onto the rim (Figs 2c and e and 3a, b, d and e). There is little evidence for melting of the projectile, or within the spall fragments, and there is no significant melt evidence along, or associated with, the crater walls. There is a large, spalled pyramidal fragment in the base of all craters at 2 and 5 km s^{-1} nominal

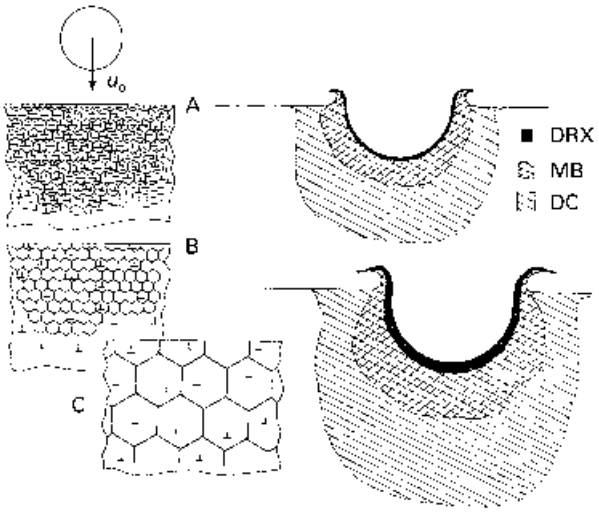

Figure 10 Schematic representation of the cratering differences observed for different starting copper target microstructures. The differences are reflected in larger craters or crater dimensions (right) in correspondingly softer targets (lower dislocation ($\perp$) density and larger grain size) (left) and variations in the extent of specific, residual. microstructural zones in the target (right). These differences, while reflecting the experimental trends observed, are exaggerated in the crater schematics (right). Shading of microstructural zones (dynamic recrystallization, DRX, microbands, MB, and dislocation cells, DC) also depicts the zone overlap, especially in the intermixing of microbands and dislocation cells. The specific, experimental targets and their characteristic microstructures are shown to the left and denoted A, B and C.

impact velocity (Fig. 2b and f). These features are quite different from the soda-lime glass impactors in Part I [1] where there was only a very small amount of glass in the crater base and no melt evidence. These features are in contrast to recent observations of soda-lime glass impact craters in 1100 aluminium targets where melt flow up the crater walls was observed, and the total volume of melt inside the crater decreased with increasing impact velocity [7]. In addition to melt phenomena for soda-lime glass sphere impacts into 1100 aluminium, there was also a significant fraction of fragmented or comminuted glass of various sizes, and at low velocities ($\sim 1\,\mathrm{km\,s^{-1}}$) the crater bottoms contained slugs of comminuted and unmelted glass [7]. Bernhard and Hörz [7] noted that the fragmentation and melting behaviour of silicate glass projectiles was complex. Correspondingly, a recent computational study of projectile melt in aluminium impactors on aluminium targets also concluded that for $8\,\mathrm{km\,s^{-1}}$ impacts there was a significant fraction of projectile material that does not reach the threshold for incipient melt [13]. Consequently, projectile behaviour is a complex issue which will require considerably more detailed analysis to begin to understand the relationships or interrelationship between melt, vaporization and spall-induced fragmentation.

In Fig. 11 we have developed several schematic views of cratering and projectile behaviour of copper

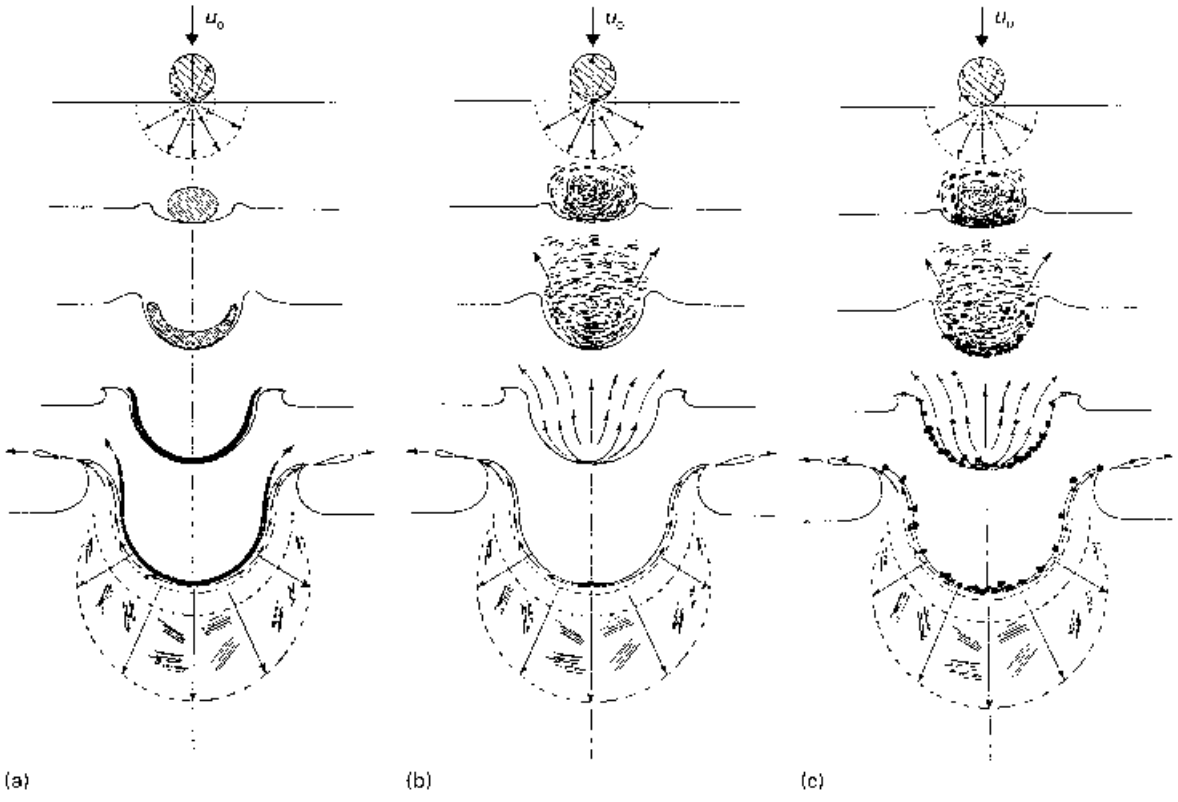

Figure 11 Crater formation and projectile behaviour schematics for same-size and varying density projectiles into the same copper target. (a) 1100 aluminium projectile impact. The projectile behaviour is dominated by melt phenomena. (b) Soda-lime glass projectile impact where the projectile fragments or vaporizes, producing no significant melt and only a small residue in the crater bottom. (c) Ferritic stainless steel projectile impact where the projectile fragments by spallation and significant quantities of fragments remain in the crater or are attached to the jetting crater wall surfaces. Clusters of lines below the crater designate microbands or other residual target microstructures or microstructure zones as in Fig. 10.

targets observed in this investigation (including Part I [1]) for soda-lime glass projectiles, ferritic stainless steel projectiles and 1100 aluminium projectiles in a recent work of Quinones *et al.* [3, 4] (see also Fig. 8). All of the projectiles represented had the same, nominal diameter, d_p, of 3.2 mm.

5. Concluding remarks

Fig. 8 provides a revealing and important summary of the effects of copper target microstructures and corresponding hardnesses on cratering over a range of impact velocities, and for significantly different projectile densities. The inclusion of the previous data of Quinones *et al.* [4] for 1100 aluminium projectiles impacting 38 μm grain size copper targets (with a corresponding hardness of 0.82 GPa) also suggests that, although the targets were softer than the experimental A targets (0.82 GPa versus 0.89 GPa), the slightly depressed p/D_c ratio values may be indicative of the significantly smaller grain size (38 μm versus 98 μm). However, the characteristic differences between the A target and the annealed B and C targets (shading in Fig. 8) attests to the significant role played by even an order of magnitude variation in dislocation density. While we have not specifically addressed the supralinearity concept [12, 14] through variations in the impactor size (or its size relative to the target grain size), we have demonstrated that the target microstructure, particularly dislocation structure, has a significant effect on cratering in copper. Consequently, it is unlikely that grain size effects in metal targets will play a significant role in cratering variations. More significant variations will likely occur for changes in dislocation structures and densities, precipitation phenomena and related microstructural features which have a significant effect on target hardness. In this respect, target hardness seems to play a dominant role in cratering and crater geometry development in copper targets.

Projectile density not only plays a significant role in the cratering process but high density ferritic stainless steel projectiles ($\rho_p = 7.86\ \mathrm{g\,cm^{-3}}$) have been shown to completely alter the cratering trends for copper targets, especially creating a low-velocity peak or maximum in p/D_c ratio values in contrast to significantly lower and continuous values for low-density, soda-lime glass projectiles ($\rho_p = 2.2\ \mathrm{g\,cm^{-3}}$). It would appear from these trends that sufficiently large values of ρ_p/ρ_t or some critically large values of projectile density relative to the target density may provoke this cratering response, since it has also been observed for aluminium projectiles impacting aluminium targets over a range of impact velocities [7, 15]. The present results for cratering in copper point out the need for many more extensive observations in other target materials, and for a wide range of projectile densities. In addition, the present experiments should be expanded to include a wider range of systematically altered target microstructures (dislocation densities, precipitation phenomena and grain size) and a wide range of projectile sizes.

The projectile behaviour observed in these experiments has been varied and complex. Little residual projectile material occurred for soda-lime glass impactors into copper while ferritic stainless steel impactors spalled profusely at $2\ \mathrm{km\,s^{-1}}$ or higher impact velocity and these spalled fragments variously remained in the craters. No significant melt phenomena were observed in connection with the projectile fragmentation or the actual cratering process and crater-related microstructures.

Initial target microstructures have a controlling effect on the residual, crater-related microstructures. Large-grain targets promote far-ranging, residual microstructures and the propensity of microbands increases with increasing target grain size. Microbands also occur in connection with very low velocity ($\sim 0.7\ \mathrm{km\,s^{-1}}$) impactors into copper targets, and microband formation is not strictly a shock-related microstructure. Shear wave effects dominate. In addition, cratering fundamentals are different for very low impact velocities and dense projectiles in contrast to hypervelocity impacts. Residual microstructure zones in copper targets associated with cratering are characterized by dynamic recrystallization extending in a narrow band from the crater wall, dislocation cells inter-mixed with microbands, or more systematic microband zones which are followed by dislocation cells which decrease in size and dislocation density with distance from the crater wall. These microstructure features establish, and are related to, hardness profiles which extend outward from the crater wall. These profiles or hardness zones (or boundaries) are generally related to the projectile density and velocity and the target microstructure. Three dimensional mappings associated with cratering in copper targets may serve to test and calibrate existing hydrocodes, and allow for more reliable extensions or extrapolations into the hypervelocity impact regime as well as applications to modelling or simulating more practical targets.

Acknowledgements

This research was supported in part by a NASA-Johnson Space Center Grant NAG-9-481 and a Mr and Mrs MacIntosh Murchison Endowed Chair (LEM) at the University of Texas at El Paso.

References

1. E. FERREYRA T., L. E. MURR and F. HÖRZ, *J. Mater. Sci.* **32** (1997).
2. M. A. MEYERS, "Dynamic Behavior of Materials" (J. Wiley & Sons, New York, 1994).
3. S. A. QUINONES, J. M. RIVAS and L. E. MURR, *J. Mater. Sci. Lett.* **14** (1995) 685.
4. S. A. QUINONES, J. M. RIVAS, E. P. GARCIA, L. E. HÖRZ and R. BERNHARD, in "Metallurgical and Materials Applications of Shock-Wave and High-Strain-Rate Phenomena", edited by L. E. Murr, K. P. Staudhammer, and M. A. Meyers (Elsevier Science, B.V., Amsterdam, The Netherlands, 1995) ch. 36, p. 293.
5. J. M. RIVAS, S. A. QUINONES and L. E. MURR, *Scripta Metall. Mater.* **33** (1995) 101.
6. S. A. QUINONES, J. M. RIVAS, E. P. GARCIA and L. E. MURR, *J. Mater. Sci.* **31** (1996) 3921.

7. R. P. BERNHARD and F. HÖRZ, *Int. J. Impact Eng.* **17** (1995) 69.
8. J. R. BAKER, *ibid.* **17** (1995) 25.
9. D. KUHLMANN-WILSDORF and L. K. IVES, *Wear* **85** (1983) 361.
10. D. A. RIGNEY, M. G. S. NAYLOR, R. DIVAKAR and L. K. IVES, *Mater. Sci. Eng.* **81** (1986) 259.
11. P. S. FOLLENSBEE, D. BANERJEE and J. C. WILLIAMS, in Proceedings of the 6th International Conference on Fracture, edited by S. P. Valluri, D. M. Taplin, P. Rama Rao, J. F. Knott and R. Dukey, New Delhi, India, Vol. 2 (Pergamon Press, Oxford, 1994) pp. 1423–1532.
12. C. J. HAYHURST, H. J. RANSON, D. J. GARDNER and N. K. BIRNBAUM, *Int. J. Impact Eng.* **17** (1995) 375.
13. M. L. ALME and C. E. RHOADES, JR, *ibid.* **17** (1995).
14. A. WATTS and D. ATKINSON, *ibid.* **17** (1995).
15. E. L. CHRISTIANSEN, *ibid* **14** (1993) 145.

Received 5 July
and accepted 23 October 1996